ACS NANO
Cite This: ACS Nano 2019, 13, 11168−11180
www.acsnano.org

ARTICLE

Differential Diagnosis and Precision Therapy of Two Typical Malignant Cutaneous Tumors Leveraging Their Tumor Microenvironment: A Photomedicine Strategy

Peiru Wang,[†,#] Weitao Yang,[†,‡,#] Shuzhan Shen,[†,#] Chao Wu,[§] Long Wen,[†] Qian Cheng,[§] Bingbo Zhang,*[,†,‡] and Xiuli Wang*[,†]

[†]Institute of Photomedicine, Shanghai Skin Disease Hospital, Tongji University School of Medicine, Shanghai 200443, China
[‡]Tongji University Cancer Center, The Institute for Biomedical Engineering and Nano Science, Tongji University School of Medicine, Shanghai 200092, China
[§]School of Physics Science and Engineering, Tongji University, Shanghai 200092, China

Supporting Information

ABSTRACT: Elevated hydrogen peroxide (H_2O_2) in biological tissues is generally recognized to be relevant to the carcinogenesis process that regulates the proliferative activity of cancer cells and the transformation of malignant features. Inspired by this observation, it can be hypothesized that imaging H_2O_2 in the tumor microenvironment (TME) could help diagnose tumor types and malignancy, and even guide precise therapy. Thus, in this study, a noninvasive photomedicine strategy is demonstrated that leverages the different levels of H_2O_2 in the TME, and two representative skin cancers, malignant melanoma (MM, clinically higher incidence of metastasis and recurrence) and cutaneous squamous cell carcinoma (cSCC, relatively less dangerous), are differentially diagnosed. The working probe used here is one we previously developed, namely, intelligent H_2O_2 responsive ABTS-loaded HRP@Gd nanoprobes (iHRANPs). In this study, iHRANPs have advantages over ratiometric imaging due to their bimodal imaging elements, in which the inherent magnetic resonance imaging (MR) mode can be used as the internal imaging reference and the H_2O_2 responsive photoacoustic (PA) imaging modality can be used for differential diagnosis. Results showed that after intravenous injection of iHRANPs, the tumor signals on both MM and cSCC are obviously enhanced without significant difference under the MR modality. However, under the PA modality, MM and cSCC can be easily distinguished with obvious variations in signal enhancement. Particularly, guided by PA imaging, photothermal therapy (PTT) can be precisely applied on MM, and a strong antitumor effect was achieved owing to the excessive H_2O_2 in the TME of MM. Furthermore, exogenous H_2O_2 was injected into cSCC to remedy H_2O_2 deficiency in the TME of cSCC, and an evident therapeutic efficacy on cSCC can also be realized. This study demonstrated that MM can be differentially diagnosed from cSCC by noninvasive imaging of H_2O_2 in the TME with iHRANPs; meanwhile, it further enabled imaging-guided precision PTT ablation, even for those unsatisfactory tumor types (cSCC) through exogenously delivering H_2O_2.

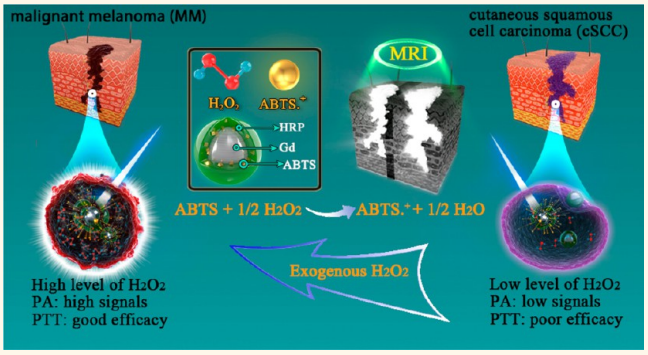

KEYWORDS: *differential diagnosis, hydrogen peroxide, malignant melanoma, cutaneous squamous cell carcinoma, photomedicine*

Skin cancers account for a growing proportion of human cancers and bring great harm to human health, and their annual incidence rate is increasing worldwide with the emergence of a population aging trend.[1−7] Considering cosmetic and functional needs that conventional pathological biopsies and surgery cannot meet, noninvasive diagnosis and precise treatment are crucial for skin tumor treatment, especially on the exposed areas. Malignant melanoma (MM), originating from melanocytes, and cutaneous squamous cell carcinoma (cSCC), originating from epidermal cells, are the most representative skin cancers.[8−10] Clinically, MM is found

Received: May 24, 2019
Accepted: October 4, 2019
Published: October 4, 2019

DOI: 10.1021/acsnano.9b04070
ACS Nano 2019, 13, 11168−11180

to be a deadly threat to patients owing to its high risk of metastasis and death,[7,10,11] while cSCC has less metastasis risk but a higher incidence.[4,6] The difference in tumor behaviors could be attributed to the tumor cell resources and the associated tumor microenvironment (TME).[12−14]

Generally, complex physicochemical structures and molecular properties of tumors lay the foundation of the TME, which further indicates the inhomogeneity in biological behaviors, such as invasiveness, malignancy, and metastasis.[15−18] Based on the previous researches, the elevated H_2O_2 level is an emerging trait in the TME that derives from organelles associated with cell oxidation, such as the cell membrane, mitochondria, and the peroxisome.[19,20] Evidence reveals that an aberrant level of H_2O_2 is closely correlated with many diseases such as cancer, especially in neoplasia initiation and progression. Thus, several cancer treatments were developed targeting elevated H_2O_2 in the cancer TME.[19−22] In addition, different levels of H_2O_2 somehow predict malignancy and different kinds of tumors. Thus, there is a great need for strategies and probes for imaging the level of H_2O_2 in the TME to help distinguish tumor malignancy and guide precise therapy.

TME-mediated multifunctional nanoprobes have attracted extensive attention recently and emerged as a promising strategy for ingenious diagnosis and precision therapies of tumors.[23−27] Recently, H_2O_2 responsive nanoprobes are reported with strong performances on imaging of H_2O_2 in serum samples and also in living organs including tumors *in vivo*. For instance, Murthy *et al.* reported on a contrast agent, peroxalate nanoparticles, with high specificity and sensitivity to detect H_2O_2 *in vivo*.[28] Zhang *et al.* reported on graphene quantum dots (GQDs) for detection of H_2O_2 in physiology and pathology.[29] Zhu *et al.* demonstrated a circulating tumor cells (CTCs)-detecting GC-Cou-Bpin nanoprobe that could rapidly respond to the high level of endogenous H_2O_2 of CTCs and capture the signal through fluorescence emission.[30] Through an electrode composed of hemin-capped biomineralized gold nanoparticles (Hem@AuNPs), reduced graphene oxide (rGO), and chitosan (CS), Li *et al.* proposed a nonenzymatic and highly electrocatalytic H_2O_2 biosensor that is ultrasensitive to detect H_2O_2 in real-time and can accurately measure H_2O_2 released from living HeLa cells.[31] Although increasing efforts have exploited these ingenious advantages of TME-based nanotechnology toward several tumor types,[26,27,32] little attention has been paid to the differential diagnosis and precision therapies of malignant tumors.

In view of the complicated characteristics of the TME, it varies largely with different types and stages of cancer; along with that, the responsiveness and applicability among different kinds of tumors are largely ignored. In light of the apparent heterogeneities in biological behavior and histopathology manifestation between MM and cSCC, the TME is predicted to be discrepant as well, which gives us an inspiration to investigate the corresponding responsiveness toward TME-mediated nanoprobes in MM and cSCC for assisting clinical diagnosis.

Just recently, intelligent H_2O_2 responsive 2,2'-azinobis(3-ethylbenzothiazoline-6-sulfonic acid) (ABTS)-loaded HRP@Gd nanoprobes (iHRANPs) were constructed that comprise photoacoustic (PA)/magnetic resonance imaging (MR) bimodes and a photothermal therapy (PTT) function *via* specific enzymatic reactions at tumor sites.[33] Results showed that iHRANPs can highly accumulate in tumors, which can be imaged by the inherent MR function of iHRANPs. Also, the accumulated iHRANPs exert a specific reaction in which ABTS is oxidized into photosensitive $ABTS^{\bullet+}$ in the presence of H_2O_2 under the catalysis of HRP for tumor-specific PA imaging and PTT treatment.[32,33]

Herein, based on the good responsiveness toward H_2O_2 and the ratiometric feature of iHRANPs, a noninvasive imaging strategy is reported to differentiate MM from cSCC under PA imaging modality, whereas the inherent MR function of iHRANPs is used as an internal imaging reference for assisting in differential diagnosis. Accurate and noninvasive diagnosis of skin cancers is crucial to their high-precision treatment. The current pathologic biopsy diagnosis and subsequent surgical excision however involve skin pricking, risk of disfigurement, and deviation from precision therapy. Due to the distinct amount of H_2O_2 in the tumor site, diverse responses to iHRANPs were exhibited in MM and cSCC. Moreover, H_2O_2-mediated PTT was conducted on MM, and it was found to have strong efficacy. For cSCC, as a H_2O_2-insufficient tumor, a sufficient treatment outcome can still be achieved *via* exogenously delivering H_2O_2. Intralesional injection is doable in skin cancer therapy.

RESULTS AND DISCUSSION

Theranostic Mechanism of iHRANPs for MM and cSCC. MM and cSCC are two representative skin cancers that can develop on any skin surface but with different degrees of malignancy.[1,2,4,6] By virtue of various epidemiological investigations and pathological studies, a large discrepancy rests in their biological behaviors, such as the degree of differentiation, malignancy phenotype and prognosis, tumor invasion, and metastasis.[1,4,6] Pathological images showed that MM tissues are kind of loose structures with a patchy distribution and vascular infiltration, while cSCC cells are clustered compactly as squamous pearls,[8,10] which indicates the heterogeneity of their TME (Figure S1, Supporting Information). Increasing evidence showed that the up-regulated H_2O_2 or the disturbances of redox homeostasis in the TME is closely correlated with cancer initiation, progression, and even the degree of malignancy.[17−19] Based on this, it can be hypothesized that MM and cSCC can be differentially diagnosed by leveraging the level of H_2O_2 in their TME.

Just recently, we developed a biomimetic H_2O_2 responsive nanoprobe, iHRANPs, which can highly accumulate in tumor lesions and sensitively detect H_2O_2 *via* PA imaging and furthermore provide PTT of tumors *in situ*.[33] When exposed to the intrinsic H_2O_2 inside the tumor, iHRANPs show potent catalytic oxidation of the loaded substrate ABTS into photosensitive counterparts, therefore enabling H_2O_2-dependent catalytic PA imaging and PTT.

In this study, inspired by the different clinical behaviors of MM and cSCC, we used iHRANPs to explore the level of intrinsic H_2O_2 inside the tumor of MM and cSCC and tried to make a differential diagnosis between them. As shown in Scheme 1, MM is a kind of H_2O_2-overexpressed skin cancer and generates much higher PA signals than cSCC (H_2O_2-insufficient skin cancers), even though they capture almost the same amount of iHRANPs. It should be noted that the comparable tumor uptake of iHRANPs by MM and by cSCC is confirmed by the inherent MR imaging function (an internal imaging reference) of iHRANPs. Thus, by recording the PA signals, we can easily distinguish MM from cSCC.

DOI: 10.1021/acsnano.9b04070
ACS Nano 2019, 13, 11168−11180

Scheme 1. Proposed schematic illustration of the H_2O_2-dependent phototheranostic mechanism of iHRANPs on MM and cSCC: a photomedicine strategy. The inherent MR imaging modality of iHRANPs is used as an internal imaging reference, and the H_2O_2-responsive PA imaging modality is used for differential diagnosis.

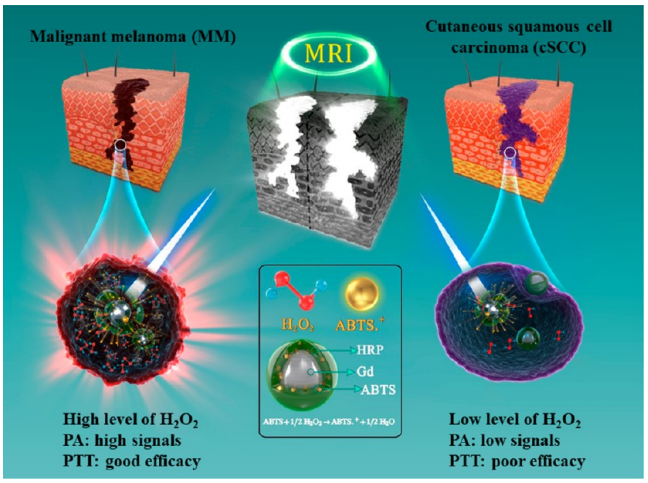

Furthermore, PTT can be precisely applied on MM with the guidance of PA imaging, and good therapeutic efficacy can be achieved owing to the high level of H_2O_2 expression in the TME. By contrast, cSCC exhibited relatively insufficient responsiveness to iHRANPs due to a low level of H_2O_2 expression in the TME. However, after exogenously adding a small quantity of H_2O_2 *via* intratumoral injection, the PA signal was significantly enhanced, and a satisfactory PTT effect was achieved, which indicates that a threshold of H_2O_2 expression in the TME may exist, and only if the threshold is reached can the corresponding PA imaging and PTT effect be triggered. Obviously, this threshold exists and is closely related to the tumor types; as such, in this study we used iHRANPs to sense it and help diagnose MM and cSCC and furthermore to exert precision PTT of them. As we know, phototheranostics has much more practicality on surface tumors such as skin cancers than on other deep solid tumors due to the penetration capability of light.[34,35]

Biomimetic Synthesis and Characterizations of iHRANPs. According to the protocol described in our previous work, iHRANPs were synthesized in a facile enzyme-biomimetic manner.[33] This synthetic strategy has many advantages: (1) The synthesis process is environmentally friendly, simple, and efficient;[36] (2) the protein coating endows nanoparticles with many favorable properties, such as high water solubility, good biocompatibility, and long half-life in blood;[37] (3) the imaging time window can be extended to hours, facilitating tumor diagnosis and imaging sensitivity.[38] Transmission electron microscopy (TEM) and dynamic light scattering (DLS) were conducted to confirm the successful

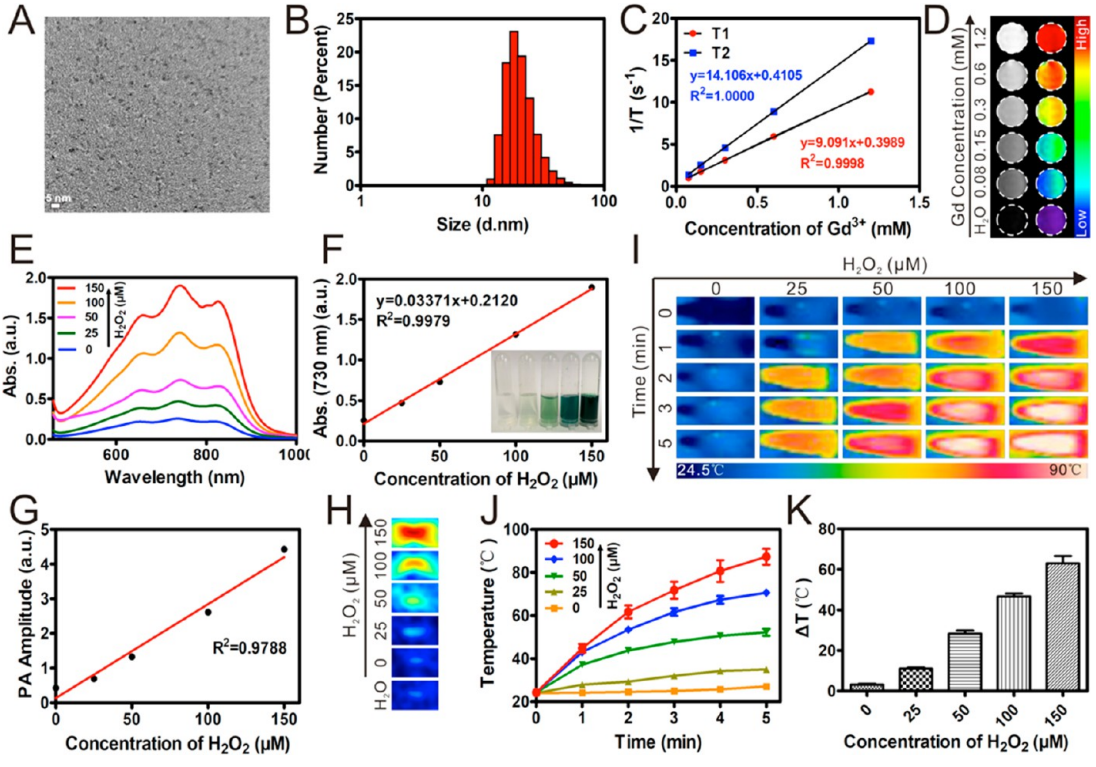

Figure 1. Characterizations and H_2O_2 responsive performance of iHRANPs. (A) Transmission electron microscopy image of iHRANPs. (B) Corresponding DLS data of iHRANPs. (C) Longitudinal and transverse relaxation fitting curves of iHRANPs. (D) *In vitro* T_1-weighted MR images of iHRANPs. (E) UV−vis absorption spectra of iHRANPs after adding different amounts of H_2O_2. (F) Linear fitted curve between H_2O_2 concentration and the absorbance at 730 nm. The inset photo is the digital picture of iHRANPs after adding different amounts of H_2O_2. (G, H) Plot of the PA intensities (G) and PA images (H) of the corresponding solutions in F. (I) Infrared thermal images of iHRANPs (5 mg/mL) with different concentrations of H_2O_2 suspensions (0 to 150 μM) in centrifuge tubes after 808 nm laser irradiation at 1 W/cm^2 for 5 min. (J) Temperature elevation curves of the corresponding samples in I. (K) Temperature increase (ΔT) varies with H_2O_2 concentration.

DOI: 10.1021/acsnano.9b04070
ACS Nano 2019, 13, 11168−11180

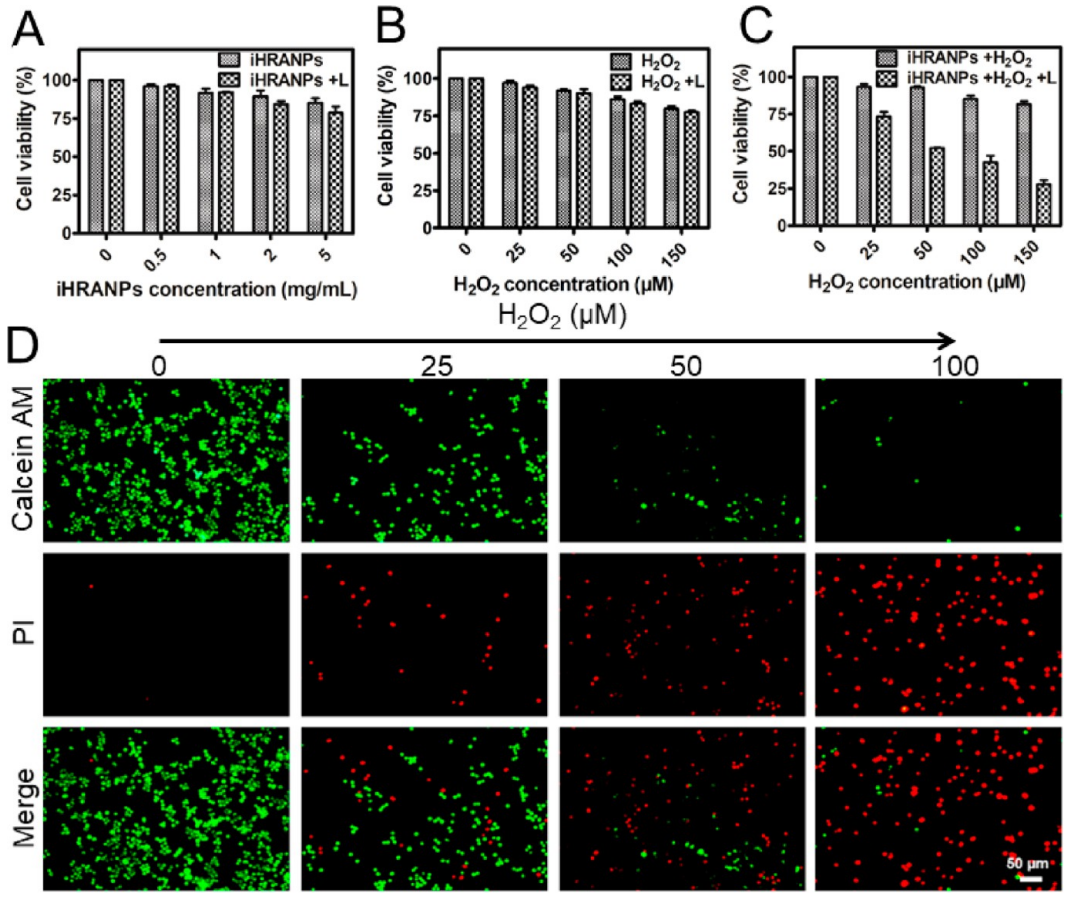

Figure 2. *In vitro* cytotoxicity and H_2O_2-dependent PTT effect of iHRANPs on B16 cells. Relative cell viability with different concentrations of iHRANPs (A), H_2O_2 (B), and iHRANPs (5 mg/mL) plus H_2O_2 (C) without *vs* with laser (808 nm, 1 W/cm^2, 5 min). (D) Fluorescence images of B16 cells costained with calcein AM (green) and PI (red). Cells were incubated with iHRANPs (5 mg/mL) and different concentrations of H_2O_2 (25, 50, 100 μM) for 24 h and irradiated with an 808 nm NIR laser at 1 W/cm^2 for 5 min. Scale bar is 50 μm.

fabrication of iHRANPs. The representative TEM image reveals the uniform spherical shape of iHRANPs with an average diameter of 4 nm (Figure 1A). The DLS size is 23 nm, which is larger than the size of TEM, due to the HRP encapsulation (Figure 1B). In addition, the T_1- and T_2-weighted MR imaging abilities of iHRANPs were evaluated by the longitudinal (T_1) and transverse (T_2) relaxation times with different Gd^{3+} concentrations (Figure 1C).[39] The longitudinal (r_1) and transverse (r_2) relaxation rates of iHRANPs were calculated to be 9.091 and 14.106 $mM^{-1}\cdot s^{-1}$, respectively. The r_2/r_1 ratio is 1.6, which is below 3, suggesting iHRANPs favor T_1-weighted MR imaging.[33,38] Subsequently, the *in vitro* T_1-weighted MR image with different Gd^{3+} concentrations (Figure 1D) further demonstrated that iHRANPs can be used as a strong T_1-weighted MR imaging contrast agent. These experimental results are highly consistent with the previously reported results. Meanwhile, the inherent T_1-weighted MR imaging capability of iHRANPs is used as an internal imaging reference for assisting differential diagnosis in this study.

H_2O_2-Dependent PA/PTT Effect *in Vitro*. The loaded ABTS in iHRANPs has slight absorption in the range of 600 and 900 nm. However, its oxidized form, namely, $ABTS^{\bullet+}$, has significant absorption in this wavelength range. As shown in Figure 1E, the absorption value increased with the increase of H_2O_2 content, which indicated the successful oxidation of ABTS and the good responsiveness of iHRANPs toward H_2O_2. The quantified linear curve between characteristic absorption value at 730 nm of iHRANPs and the H_2O_2 content is also provided in Figure 1F. Due to the NIR absorption of the oxidized form of $ABTS^{\bullet+}$, iHRANPs showed H_2O_2-dependent PA imaging behavior, as shown in Figure 1G and H. What is more, the PA signal of iHRANPs itself showed no difference with pure water, a linear increase with the increase of H_2O_2 concentration (R^2 = 0.9788), which suggested the perfect PA imaging property of iHRANPs in the presence of H_2O_2.

The *in vitro* photothermal conversion effect of iHRANPs was further measured. It can be found that the temperature increase of iHRANPs alone is negligible, which is not enough to kill cancer cells; however, when H_2O_2 was added into the aqueous solution, the temperature reaches approximately 60 °C (Figure 1I and J), which is sufficient to kill tumors.[40] Meanwhile, the temperature increase (ΔT) also had a positive relation with the concentration of H_2O_2, which was a benefit to adjust the photothermal effects *in vitro* and *in vivo* (Figure 1K). Moreover, iHRANPs had good photostability, showing that the temperature can reach almost the same peak under 808 nm laser irradiation (1 W/cm^2) for four cycles (Figure S2, Supporting Information), which is more stable than NIR organic dyes.[41,42] The results of *in vitro* experiments indicated the good feasibility of iHRANPs for sensing H_2O_2 in the TME of MM and cSCC and guiding photothermal therapy.

Cytotoxicity and H_2O_2-Dependent PTT Effect of iHRANPs on Cells. Before exploring photothermal therapy

DOI: 10.1021/acsnano.9b04070
ACS Nano 2019, 13, 11168−11180

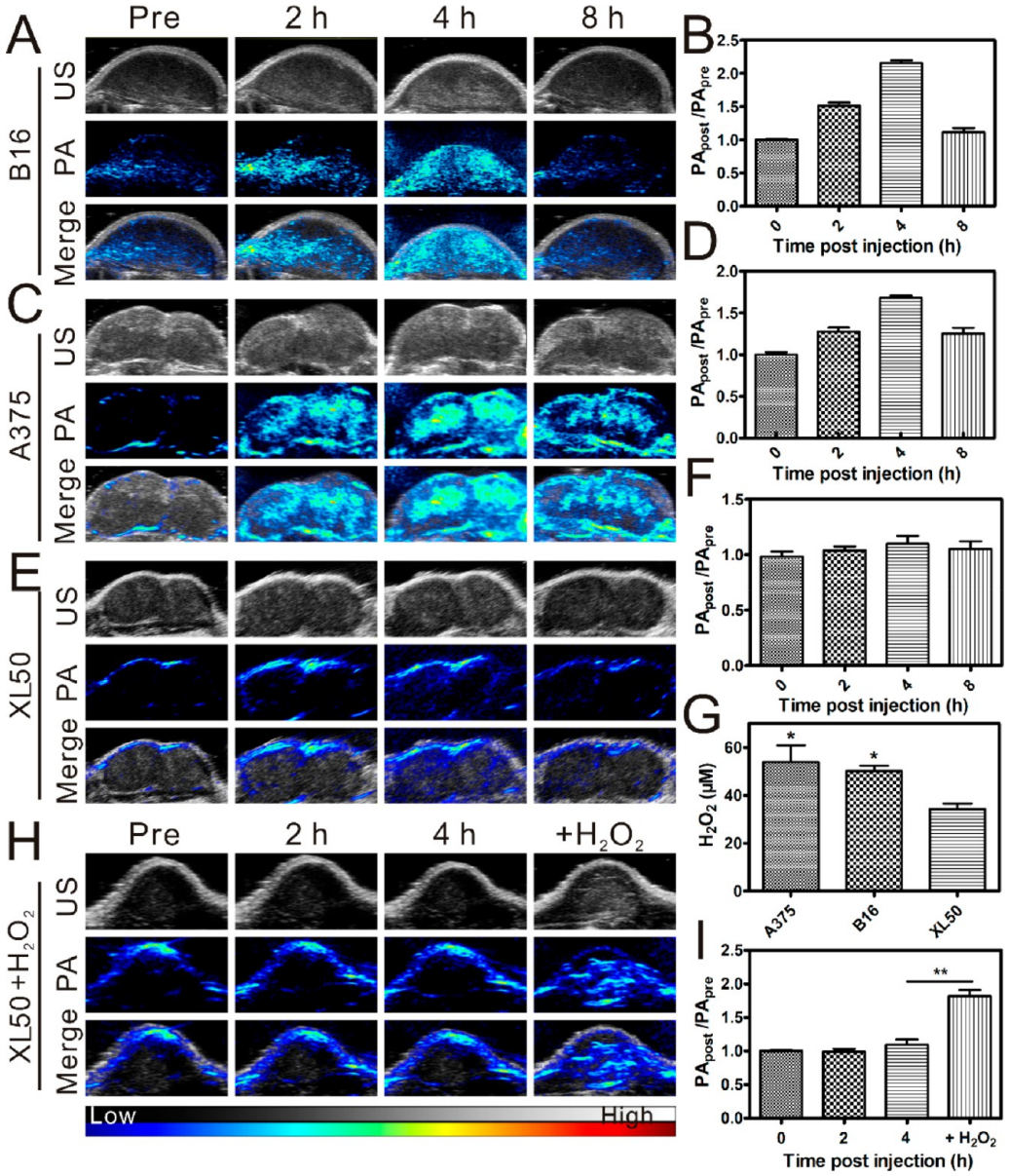

Figure 3. Distinct performance of TME-responsive PA imaging on MM and cSCC mice models. PA images, ultrasound (US), and the merged images of MM-B16 (A), MM-A375 (C), and cSCC-XL50 (E) before and 2, 4, and 8 h after intravenous injection of iHRANPs. (B, D, F) Corresponding PA intensities of those in A, C, and E. (G) Contents of H_2O_2 in tumor tissues from MM (B16 and A375) and cSCC (XL50) mice. (H) PA images, US, and the merged images of cSCC (XL50) tumor before and 2 and 4 h after intravenous injection of iHRANPs and with exogenously injecting 20 μL of H_2O_2 (100 μM) *in situ* at 4 h postadministration. (I) Corresponding PA intensities of those in H. *p < 0.05, **p < 0.01.

in vivo, we evaluated the *in vitro* biocompatibility of iHRANPs. Cell experiments including the cytotoxicity and anticancer effect of iHRANPs were conducted on three skin cancer cell lines by standard CCK-8 assay. As shown in Figure 2A and B, either iHRANPs (0, 0.5, 1, 2, 5 mg/mL) themselves or H_2O_2 (0, 25, 50, 100, 150 μM) itself exhibited negligible cytotoxicity in the absence of laser irradiation, which indicated the good biocompatibility of iHRANPs and H_2O_2 in the investigated concentration range. These results do not vary with the type of cell line (cSCC-derived cells or MM-derived cells) (Figures S3 and S4, Supporting Information).

The combinations of iHRANPs plus H_2O_2, iHRANPs plus laser, and H_2O_2 plus laser showed no additive cytotoxicity effect on cells. However, with 808 nm laser irradiation, the group of iHRANPs plus H_2O_2 displays prominent anticancer capability; meanwhile, it was found that with the increase of H_2O_2 concentration, the cell killing effect was increased (Figure 2C, Figures S3 and S4, Supporting Information). Calcein/propidium iodide staining was further used to identify the apoptosis, and the results are shown in Figure 2D. It becomes obvious that the combination of iHRANPs (5 mg/mL) plus 100 μM H_2O_2 plus illumination (808 nm, 1 W/cm^2, 5 min) group showed the maximum number of apoptotic cells. *In vitro* cell experiments revealed the strong H_2O_2/laser-dependent PTT effect of iHRANPs; however, only iHRANPs were nontoxic to cells.

The above H_2O_2-selective PA imaging/PTT effect and the good biocompatibility collectively suggested that iHRANPs can be a good candidate for differential diagnosis and precision

DOI: 10.1021/acsnano.9b04070
ACS Nano 2019, 13, 11168−11180

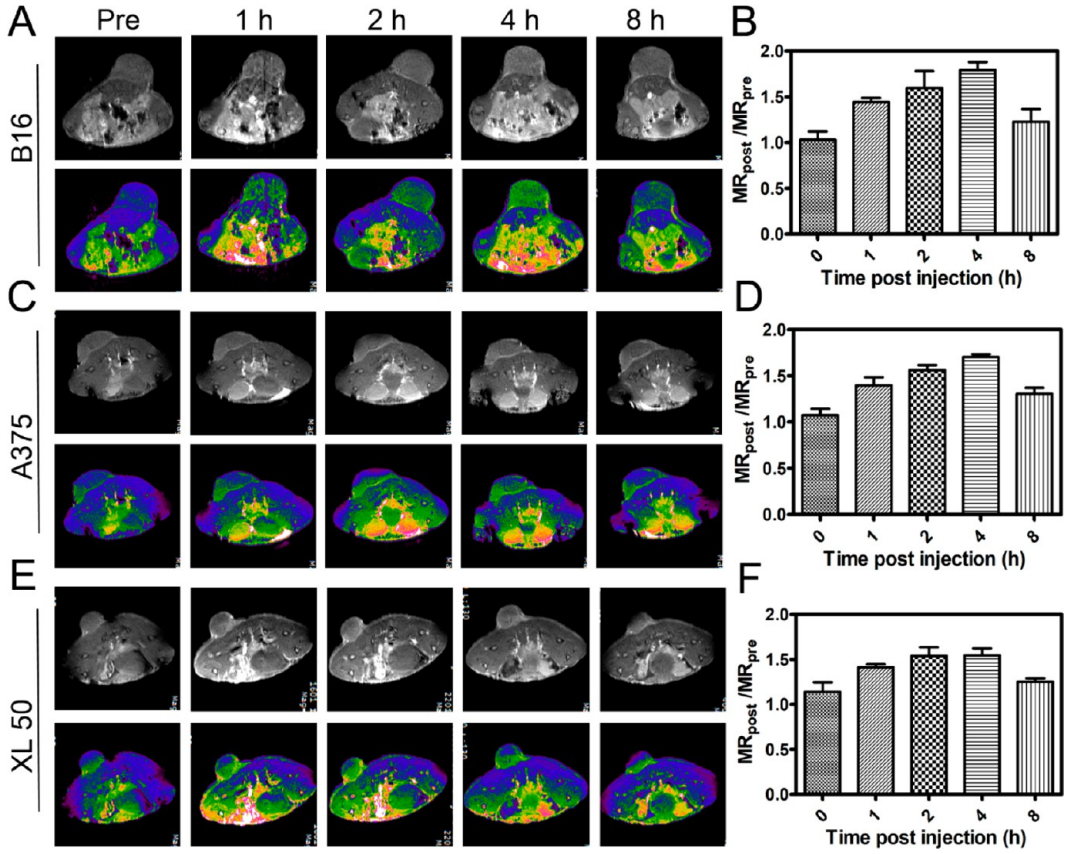

Figure 4. MR imaging modality of iHRANPs as an internal reference for assisting differential diagnosis of MM from cSCC. T_1-weighted MR imaging of MM-B16 (A), MM-A375 (C), and cSCC-XL50 (E) tumors before and 1, 2, 4, and 8 h after iHRANPs i.v. injection (dose: 0.12 mmol Gd/kg). (B, D, F) Corresponding ratio values of T_1-weighted MR signal intensity of tumors before and after i.v. injection of iHRANPs at different time points.

therapy of malignant cutaneous tumors by leveraging their tumor microenvironment.

Differential Diagnosis of MM from cSCC by iHRANPs *in Vivo*. Leveraging the selectivity and sensitivity of iHRANPs toward H_2O_2, *in vivo* PA imaging on two MM tumor models (B16 and A375) and one cSCC tumor model (XL50) was conducted by intravenous injection of iHRANPs, aiming to distinguish MM from cSCC. Figure 3 clearly showed that much higher PA signals on the two kinds of MM mice are obtained compared with that on the cSCC mice. Specifically, a time-dependent enhancement of the PA signal intensity in the tumor areas of B16 and A375 mice was observed within the first 4 h postinjection. The B16 and A375 tumor-bearing mice exhibit 2.35-fold and 1.74-fold enhancement at 4 h post-injection in the tumor region, respectively (Figure 3B and D). Interestingly, the PA signals on B16-bearing mice were much more homogeneous than that on A357 tumor-bearing mice, and the size and the basic structure of the tumor region can be clearly seen by PA imaging. As expected, no obvious augmentation of the PA signal was observed on cSCC mice (XL50) (Figure 3E and F). This significant difference in PA signal generation of iHRANPs on MM and cSCC could be mainly attributed to the accumulated amounts of iHRANPs and also the H_2O_2 levels in their tumor areas.

In order to exclude the negative influence of the accumulation of iHRANPs, MR imaging as an internal reference was performed on these three mice tumor models. Figure 4 shows that iHRANPs could target all three tumor lesions without significant statistical difference. Moreover, it can be seen that the MR signal in the tumor was gradually enhanced postinjection and reaches a maximum at 4 h postinjection. The quantified ratios of MR_{post}/MR_{pre} on MM mice (B16, A375) and cSCC mice (XL50) were also provided, and the ratio value at 4 h postinjection is located in the range of 1.5−2.0. The internal imaging reference by MR imaging modality on all three tumor models indicated that the accumulated amounts of iHRANPs in these three tumor models were almost the same. Particularly, the enhancement trend under the MR imaging modality was fairly consistent with that under the PA imaging modality. From the above results, the more enhanced PA signals in MM were mainly contributed from the higher level of H_2O_2 in the TME of MM.

To further confirm the variations of H_2O_2 in the TME of MM and cSCC, the concentrations of H_2O_2 in these three tumor tissues were quantitatively determined. Specifically, the H_2O_2 concentrations in the tumor tissues of A375, B16, and XL50 were found to be 53, 51, and 36 μM, respectively. Broadly, the H_2O_2 level in MM was significantly higher than that in cSCC (Figure 3G). These results are well consistent with pathological features (Figure S1, Supporting Information) and particularly with PA imaging characteristics, suggesting MM can be differentially diagnosed in a noninvasive manner from cSCC by using iHRANPs under the PA imaging modality (Scheme 1).

It is worth noting that an apparent PA signal enhancement (1.895-fold) was observed on cSCC mice (XL50) after

DOI: 10.1021/acsnano.9b04070
ACS Nano 2019, 13, 11168−11180

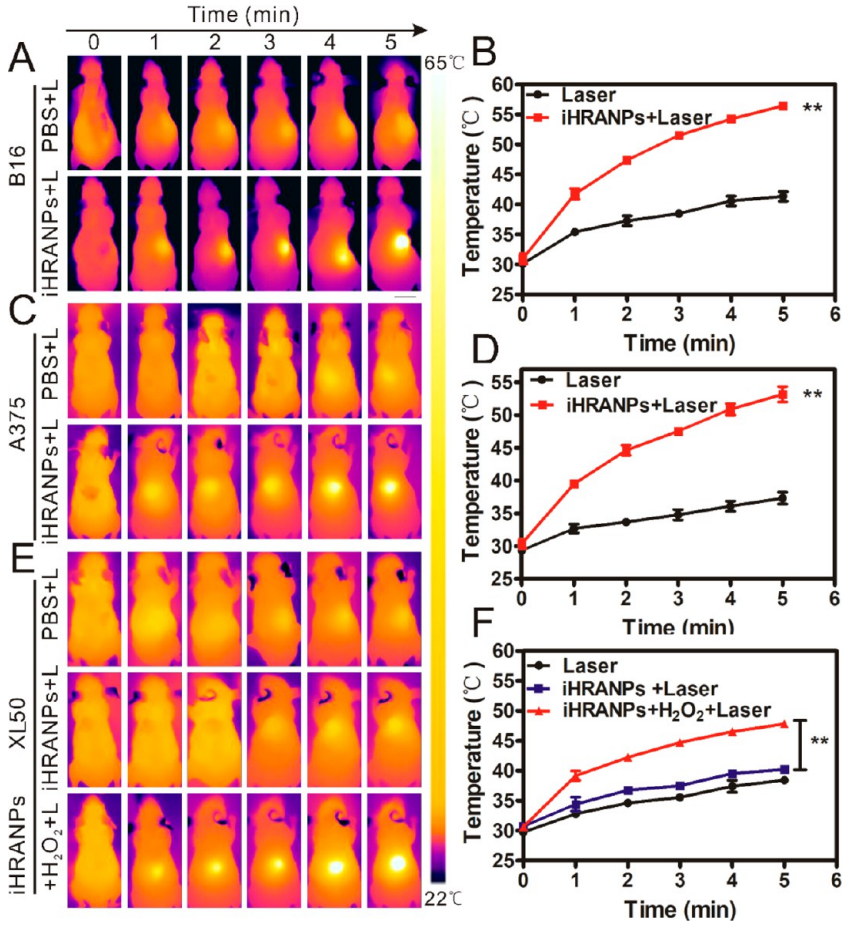

Figure 5. H_2O_2 responsive photothermal efficiency evaluation of iHRANPs on MM and cSCC. Infrared thermal images of MM-B16 (A), MM-A375 (C), and cSCC-XL50 (E) mice captured at designated times under 808 nm laser (1 W/cm^2) irradiation for 5 min. The cSCC-XL50 mice *in situ* injected with 20 μL of H_2O_2 (100 μM) were taken as a supplement control. (B, D, F) Temperature variation curves of tumor sites recorded in A, C, and E, correspondingly. **$p < 0.01$.

exogenous injection of 20 μL of H_2O_2 (100 μM) into the tumor at 4 h postadministration of iHRANPs (Figure 3H and I). These results demonstrate that the PA signal of the tumor was closely related to the content of H_2O_2 within the tumor, regardless of whether the H_2O_2 originated endogenously or exogenously. Thus, iHRANPs-mediated PA imaging, with a preferable spatial and high-resolution and noninvasive feature,[40−43] provided a promising imaging technique to detect H_2O_2 *in vivo* and further assisted with the differential diagnosis between MM and cSCC.

H_2O_2 Responsive Precision Therapy of MM by iHRANPs *in Vivo*. By leveraging the variations of H_2O_2 in the TME of MM and cSCC, iHRANPs showed good performance in distinguishing them under the PA imaging modality. In addition to the differential diagnosis, MM can be precisely eliminated by iHRANPs since the overexpressed H_2O_2 in the TME can trigger catalytic oxidation, generating a large number of photosensitive $ABTS^{\bullet+}$, which had good photothermal conversion efficiency. To further evaluate the precision PTT efficacy of iHRANPs *in vivo*, mice were divided into four groups, iHRANPs + laser (iHRANPs + L), laser only (L), iHRANPs only (iHRANPs), and phosphate-buffered saline (PBS). According to the results of the PA and MR imaging above, iHRANPs accumulate and reach a peak at 4 h postinjection; thus tumors received laser illumination (808 nm, 1 W/cm^2, 5 min) at 4 h postinjection. As revealed in Figure 5A−D, the temperatures of the tumor sites on MM mice (B16, A375) treated with iHRANPs + L increased significantly up to *ca.* 55 °C after irradiation for 5 min, while the temperatures of the tumor sites on cSCC (XL50) treated with iHRANPs + L just increased from 30 °C to 39 °C. Mice exposed to laser only were regarded as a control, and the temperatures were all found to be below 40 °C after laser irradiation for 5 min. It has been widely demonstrated that hyperthermia over 50 °C can cause cancer cell necrosis.[12,20] Predictably, a good photothermal effect was achieved on MM mice and a poor one was found on cSCC-XL50 mice. It should be noted that there was an approximately 10 °C of increase on MM-B16 mice only with laser irradiation, which is probably due to the absorption of NIR by melanin (Figure 5B), while a negligible temperature variation was observed on MM-A375 and on cSCC-XL50 mice.

Interestingly, by exogenous injection of 20 μL of H_2O_2 (100 μM) into the tumor site to replenish H_2O_2 in cSCC-XL50 mice, as expected, the temperature dramatically increased by nearly 25 °C (Figure 5E and F). This finding emphasized the crucial role of H_2O_2 in the TME in our theranostic strategy, and based on the PA imaging we can exert precision PTT on MM. It was also reported that combining this with other strategies, such as glucose oxidase (GOx) and superoxide dismutase (SOD), could increase the H_2O_2 amount and

DOI: 10.1021/acsnano.9b04070
ACS Nano 2019, 13, 11168−11180

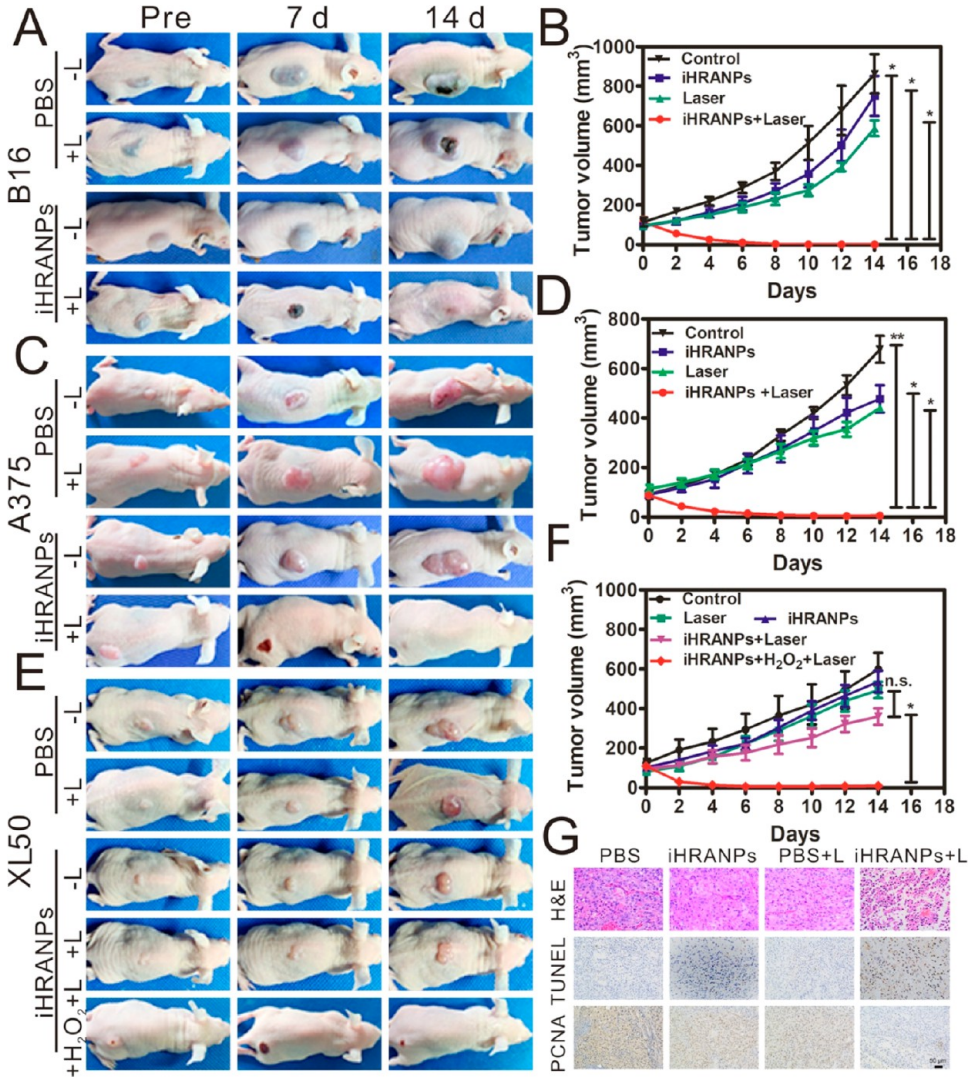

Figure 6. H_2O_2 responsive precision PTT of MM and cSCC *in vivo*. Representative photos of MM-B16 (A), MM-A375 (C), and cSCC-XL50 (E) mice before treatment and at day 7 and day 14 after treatment. Tumor growth curves of MM-B16 mice (B), MM-A375 mice (D), and cSCC-XL50 mice (F) after treatment. The cSCC-XL50 mice *in situ* injected with 20 μL of H_2O_2 (100 μM) were taken as a supplement control (*$p < 0.05$, **$p < 0.01$ and n.s. represents no significance). (G) Histological analysis of tumor slices with H&E, TUNEL, and PCNA staining at day 14 in different groups. The brown color indicates the TUNEL or PCNA signals, and the cell nuclei were stained blue (200×, scale bar: 50 μm; applies to all images).

improve the theranostic effect when H_2O_2 is insufficient in the TME.[44,45]

After recording the real-time temperatures of tumor sites, precision PTT was conducted on MM. Figure 6 shows that the tumor volumes on B16- and A375-bearing mice (MM) continuously decrease and then disappear at day 5 post-treatment in the group of iHRANPs + L, while there was no significant suppression of tumor volume in other groups (iHRANPs, L, and PBS). Predictably, unsatisfactory PTT efficacy was found on XL50-bearing mice (cSCC). These different therapeutic effects of iHRANPs on MM and cSCC were consistent with the *in vivo* PA imaging results above and ultimately with the H_2O_2 level in the tumor site.

In order to achieve good PTT efficacy on cSCC, an additional amount of H_2O_2 was locally injected into the XL50 tumor (cSCC); then the tumor can be distinctly suppressed (Figure 6E and F). Compared with the nonsupplement group, by additional injection of H_2O_2 it also achieved good PTT efficacy, which further confirmed that H_2O_2 in the tumor site plays an essential role in precision PTT.

To further explore the therapeutic outcome, B16-bearing mice in different groups were sacrificed on day 14, and the tumor tissues were collected for histological analysis (Figure 6G). Compared with the other groups, more severe cell damage was found in the iHRANPs + L group with hematoxylin−eosin (H&E) staining of the tumor slices. These results were consistent with the TdT-mediated dUTP nick-end labeling (TUNEL) staining assay. Apoptotic cells in tumor tissue significantly increased in the iHRANPs + L group. Proliferating cell nuclear antigen (PCNA) staining results also indicated that the proliferation capacity of tumor cells is prominently inhibited in the iHRANPs + L group. These analysis results together confirmed the potent photothermal therapeutic efficacy of iHRANPs, and this treatment is H_2O_2-dependent (Figure 6).

***In Vivo* Biodistribution and Toxicology Analysis.** Before the toxicity evaluation, the biodistribution of iHRANPs

DOI: 10.1021/acsnano.9b04070
ACS Nano 2019, 13, 11168−11180

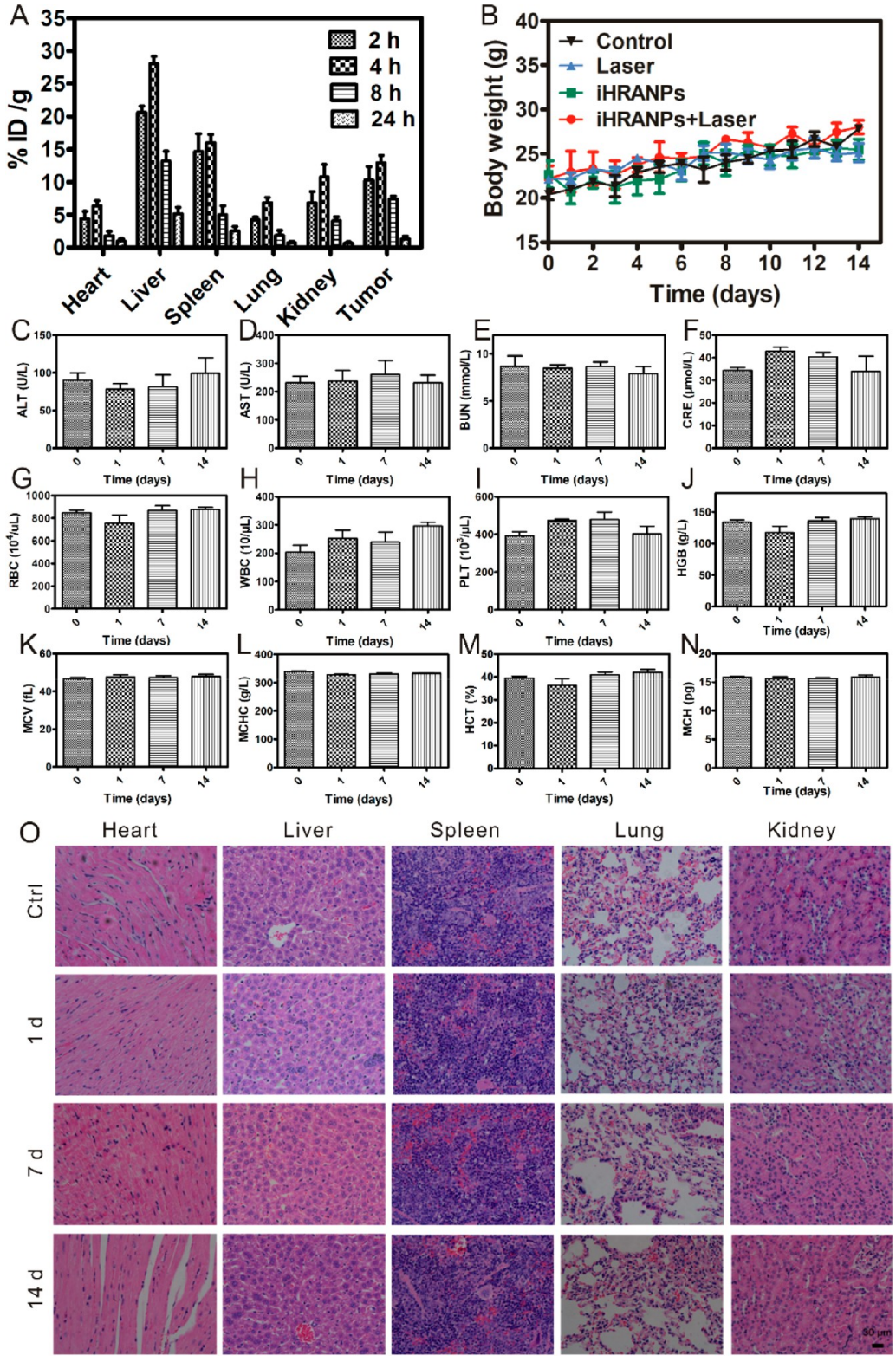

Figure 7. ***In vivo*** **biodistribution study and biosafety evaluation of iHRANPs** ***via*** **intravenous injection. (A) Biodistribution of Gd (% injected dose (ID) of Gd per gram of tissues) in main tissues and tumor at 2, 4, 8, and 24 h after i.v. injection of iHRANPs. (B) Change in body weight in each group after various treatments during 14 days. (C−N) Values of serum AST, ALT, CRE, and BUN and routine blood examination on days 0, 1, 7, and 14 in different groups (*** n **= 3). (O) H&E staining of the major organs (heart, liver, spleen, lung, and kidney) dissected from the mice intravenously injected with iHRANPs at different time points (200×, scale bar: 30** μ**m; applies to all images).**

on tumor-bearing mice was measured (Figure 7A). It can be observed that iHRANPs are primarily distributed in the spleen and liver on account of the reticuloendothelial system capture. It should be noted that the tumor uptake of iHRANPs is determined to be 14.35% (measured by Gd^{3+}) of the injected dose per gram tissue (% ID/g) at 4 h postinjection (Figure

DOI: 10.1021/acsnano.9b04070
ACS Nano 2019, 13, 11168−11180

7A). This high tumor uptake was mainly attributed to the ultrasmall size of iHRANPs and the protein encapsulation.[33]

The potential toxicity was evaluated through body weight monitoring, blood tests, and H&E staining of major organs. As shown in Figure 7B, no loss of body weight was observed in any group during the treatment. Routine blood tests and serum biochemistry tests (AST, ALT, BUN, and CRE) were conducted to assess the toxicity of iHRANPs *in vivo*. The amounts of AST, ALT, BUN, and CRE were not significantly different at 1, 7, and 14 days after iHRANPs i.v. injection from those preinjection, which indicates that there was no hepatic or renal dysfunction induced by iHRANP injection (Figure 7C–F). Likewise, the results of routine blood examination also appeared to be normal (Figure 7G–N). Besides, no evident tissue damage or side effect was observed in major organs (heart, liver, spleen, lung, and kidney) after systemic administration of iHRANPs (Figure 7O). Thus, all these results demonstrated that iHRANPs have low toxicity and could be transferred for clinical use.

CONCLUSIONS

In summary, iHRANPs, an intelligent biomimetic theranostic nanoprobe with a special structure, not only demonstrated good performance on differentiating MM from cSCC under PA imaging modality but also further exerted a potent and precision tumor killing effect with NIR laser irradiation by leveraging their different levels of H_2O_2 in the TME. The inherent MR imaging modality of iHRANPs as an internal imaging reference showed iHRANPs can highly accumulate in the tumor sites of both MM and cSCC, but iHRANPs in MM tumor enabled much higher PA signals than that in cSCC tumor. This difference in PA signals was attributed to the different levels of H_2O_2 in the TME of MM and cSCC confirmed by H_2O_2 detection. As such, based on PA imaging, we demonstrated the feasibility of differential diagnosis of MM from cSCC. Moreover, guided by PA imaging, precision PTT treatment was conducted on MM that contained overexpressed H_2O_2 in the TME. For cSCC with a low level of H_2O_2 in the TME, by exogenously delivering H_2O_2 we can also achieve a good tumor-specific PTT effect. Therefore, the present investigation proposes an interesting concept not only for preliminary differential diagnosis but also for further imaging-guided precision treatment in dermatology.

EXPERIMENTAL SECTION

Materials. ABTS, HRP, $GdCl_3{\cdot}6H_2O$, and sodium hydroxide solution (NaOH) were obtained from Aladdin Co. Ltd. (Shanghai, China). Cell culture media, streptomycin, fetal bovine serum (FBS), and penicillin were purchased from Gibco, Invitrogen Corp. (Carlsbad, CA, USA). B16 (murine malignant melanoma) and A375 (human malignant melanoma) cell lines were obtained from Boster Biological Technology Co. Ltd. (Wuhan, China). Murine squamous cell carcinoma cell line XL50 was established from UV-induced squamous cell carcinoma in SKH-1 hairless mice. A live–dead cell viability assay kit (Calcein AM/PI) and Cell Counting Kit-8 (CCK-8) were acquired from Beyotime Institute of Biotechnology (Nanjing, China).

Fabrication and Characterizations of iHRANPs. In this work, iHRANPs were fabricated according to a protein-mediated biomimetic synthesis strategy.[33,43,44] In short, HRP (10 mg) was dissolved in 1 mL of ultrapure water, and a $GdCl_3{\cdot}6H_2O$ (50 μL, 100 mM) solution was added and stirred at 37 °C for 5 min. After that, NaOH (50 μL, 1.0 M) was added into the above system, and the pH of solution was adjusted to 12. Subsequently, the above solution was stirred for 6 h at physiological temperature (37 °C). Then the whole solution was purified by dialysis for 24 h. After purification, 8 mg of ABTS was added into the solution, which was stirred overnight in the dark. Finally, iHRANPs were obtained after purification by ultrafiltration and rinsed at least three times. The resulting iHRANPs were weighed after lyophilization and stored at 4 °C until further use.

TEM was used to analyze the size and the morphology of iHRANPs. DLS was utilized to measure the average hydrodynamic size of iHRANPs. The UV–vis absorbance spectrum of each sample was carried out on a Cary 60 UV–vis spectrometer (Agilent, USA). The relaxation times of iHRANPs, including T_1 and T_2, were detected at 37 °C by a Bruker MR analyzer. T_1-weighted MR images were captured using a clinical MR imaging system (3.0 T, Philips).

***In Vitro* H_2O_2 Response and Photothermal Effect Evaluation.** In a typical procedure, different concentrations of H_2O_2 ranging from 0 to 150 μM mixed with iHRANP (5 mg/mL) solutions were added into a centrifuge tube (0.6 mL) at 37 °C, respectively. The above samples received irradiation for 5 min using an 808 nm NIR laser (1 W/cm^2). The temperatures and thermal images of these solutions were recorded by an infrared thermal imaging camera (Shanghai Kewang Industrial Co., Ltd.) at 1 min intervals.

***In Vitro* PA Imaging.** *In vitro* PA imaging was implemented as follows. Polyethylene capillaries were filled with iHRANPs solutions with different concentrations of H_2O_2 and H_2O, respectively, and then placed on the coupling gel for PA imaging (Vevo LAZR, FujiFilm VisualSonics, Japan). Both PA and ultrasound signals were monitored, and the wavelength of laser irradiation for PA imaging was 730 nm. The PA intensities of regions of interest were calculated for quantification analysis.

***In Vitro* Cell Viability Assay.** A375 and XL50 cells were cultured in DMEM medium (Gibco, Thermo Fisher Scientific, Germany) supplemented with 10% FBS (Biochrom AG, Germany) and 100 μg/mL penicillin, while B16 cells were cultured in RPMI medium (Gibco, Thermo Fisher Scientific, Germany). All cells were kept under standard conditions (37 °C in a humidified atmosphere of 5% CO_2).

For the *in vitro* cytotoxicity assay, B16 cells were plated into 96-well plates and incubated overnight to allow the attachment of cells. Subsequently, serial concentrations of iHRANPs (0, 0.5, 1, 2, 5 mg/mL) were added and incubated for 24 h. Using the CCK-8 method, toxicity examination of iHRANPs was performed on all cell lines. Moreover, dark cytotoxicity and phototoxicity of pure H_2O_2 with various concentrations (0, 25, 50, 100, 150 μM) and the mixtures of H_2O_2 (0, 25, 50, 100, 150 μM) with iHRANPs (5 mg/mL) were also detected by the CCK8 assay.

For phototoxicity measurement, B16 cells were exposed to 808 nm laser irradiation for 5 min under 1 W/cm^2. The following formula was applied to calculate the cell viability: cell viability (%) = $[(A_s - A_b)/(A_c - A_b)] \times 100\%$, where A_s, A_b, and A_c represent the OD 450 of the treatment group, blank well, and control group, respectively. The experiments were performed thrice. The cytotoxicity assays on A375 and XL50 cells were also performed.

***In Vitro* Apoptosis Assay.** The *in vitro* apoptosis assay was performed using live and dead cell assessment. B16 cells were plated into a 24-well plate (0.5×10^4 cells/well) for 24 h. Then iHRANPs (5 mg/mL) were added into the culture medium in the presence of various concentrations (25, 50, 100 μM) of H_2O_2. The iHRANPs without H_2O_2 were used as a control group. After 6 h of incubation in the dark, the cells were irradiated under an 808 nm laser (1 W/cm^2, 5 min). After another 40 min of incubation in the dark, the cells were washed with PBS twice and stained with calcein-AM (2 μM) and PI (8 μM). Then apoptotic cells were detected by fluorescence microscope (Olympus ix53) to observe the cell apoptosis. Live cells were determined as green-fluorescent calcein AM (ex/em: 495/520 nm), while dead cells were identified by propidium iodide (ex/em: 530/620 nm), which emit red fluorescence once combined with the nucleic acids of the damaged cells.

***In Vivo* PA/MR Dual-Modality Imaging.** The animal protocols were evaluated and approved by the Animal Laboratory Ethics Committee of Tongji University. Female 5–6-week-old nude mice were purchased from Qianbi Biological Technology Co. Ltd.

DOI: 10.1021/acsnano.9b04070
ACS Nano 2019, 13, 11168–11180

(Shanghai, China). Xenograft mouse models with B16, A375, and XL50 tumors were prepared by subcutaneous injection of 1×10^6 B16 cells, 1×10^6 A375 cells, and 5×10^6 XL50 cells (suspended into 100 μL of PBS) into the flank region of each nude mouse. When the tumor volume was close to 100−200 mm^3, mice were treated with iHRANPs *via* i.v. injection (200 μL). After anesthetization with 5% isoflurane, tumor-bearing mice were imaged with PA and MR.

In vivo MR imaging was conducted on a clinical MR imaging system (3.0 T, Philips). Briefly, the tumor-bearing mice (B16, A375, XL50) were scanned before and after iHRANPs i.v. injection (dose: 0.12 mmol Gd/kg) at 1, 2, 4, and 8 h postinjection. The MR imaging parameters were field of vision (FOV) read: 90 mm, TR/TE: 600 ms/20 ms, FOV phase: 90 mm, slice pos: 11.8, slice thickness: 3.5 mm, ST: 1.2, slice gap: 0.5 mm, flip angle: 90°, axial orientation SE (spin echo). Quantification of MR signals at tumor sites was implemented by ImageJ software.

For *in vivo* PA imaging, the tumor-bearing mice (B16, A375, XL50) were scanned on an animal photoacoustic imaging system (Vevo LAZR, FujiFilm VisualSonics, Japan) before and after i.v. injection of 200 μL of iHRANPs (5 mg/mL) at different time points (2, 4, and 8 h after injection).

For exogenous injection of H_2O_2 in cSCC mice (XL50), we multiply injected 20 μL of H_2O_2 (100 μM) into the tumor using a microsyringe at 4 h postadministration of iHRANPs.

H_2O_2 Determination. The content of H_2O_2 in the tumor tissues derived from the above tumor-bearing mice (B16, A375, and XL50) was determined using a commercially available ELISA (enzyme-linked immunosorbent assay) kit (eBioscience, CA, USA). All samples were measured in duplicate, and the mean concentration was calculated.

***In Vivo* PTT Ablation of MM and cSCC.** PTT efficacy *in vivo* was evaluated on B16, A375, and XL50 tumor-bearing mice. Tumor-bearing mice were divided into four groups, namely, iHRANPs + laser, iHRANPs only, laser only, and PBS, respectively. Each group had three mice.

In vivo photothermal efficiency of iHRANPs was detected using an infrared thermal imaging camera. At 4 h postinjection of iHRANPs, tumors were irradiated by an 808 nm laser for 5 min (1 W/cm^2). The infrared thermographic images and the temperatures of tumor sites were recorded at 1 min intervals. During the treatment, the sizes of tumors were measured every other day, and the volumes were calculated according to the following equation: volume = $(a) \times (b)^2/2$ (a: tumor length, b: tumor width). Two weeks after various treatments, mice were sacrificed for histological analysis. The tumor tissue sections were further analyzed with H&E, TUNEL, and PCNA assays.

Biodistribution and Pharmacokinetics Analysis of iHRANPs. When subcutaneous tumors grew up to 100−200 mm^3, the mice were intravenously injected with iHRANPs (200 μL per mouse, 5 mg/mL). The tumor-bearing mice were sacrificed 2, 4, 8, and 24 h after injection. The main organs (spleen, heart, kidney, liver, and lung) and tumors were collected and weighed. The collected tissues were treated with aqua regia. Then, the Gd content in each melted sample solution was analyzed using an Agilent 725 ICP-OES. Finally, the biodistribution of iHRANPs based on Gd was obtained *via* the percentage of injected dose per gram of tissue (% ID/g).

For pharmacokinetics analysis, the mice were intravenously injected with iHRANPs (200 μL per mouse, 5 mg/mL). A 100 μL amount of blood was collected from the mouse orbit at different time points postinjection (0.5, 1, 2, 4, 6, 8, 24 h). The blood samples were treated with aqua regia. Then, the Gd content in each sample solution was analyzed using Agilent 725 ICP-OES. Finally, the pharmacokinetics of iHRANPs based on Gd was obtained *via* the percentage of injected dose per milliliter (% ID/mL). The blood retention of iHRANPs was decreased to 1.67 ± 2.08% ID/mL at 24 h postintravenous injection (Figure S5, Supporting Information).

***In Vivo* Toxicity Evaluation of iHRANPs.** The body weight of the mice was measured every other day to evaluate the side effects of iHRANPs after administration. Healthy nude mice intravenously injected with iHRANPs (200 μL/mouse, 5 mg/mL) were sacrificed for blood collection and H&E staining of major organs (spleen, heart, kidney, liver, and lung,). The blood levels of red blood cells (RBC), white blood cells (WBC), hemoglobin (HGB), hematocrit (HCT), mean corpuscular volume (MCV), mean corpuscular hemoglobin concentration (MCHC), mean corpuscular hemoglobin (MCH), and platelets (PLT) were measured before and after injection. Serum biochemistry data including blood urea nitrogen (BUN), aspartate aminotransferase (AST), alanine aminotransferase (ALT), and creatinine (CRE) were tested. Data obtained from untreated mice were considered as control.

ASSOCIATED CONTENT

Supporting Information

The Supporting Information is available free of charge on the ACS Publications website at DOI: 10.1021/acsnano.9b04070.

Supplemental figures showing histopathologic images of MM and cSCC, photothermal stability of iHRANPs, *in vitro* cytotoxicity and H_2O_2-dependent PTT effect of iHRANPs on A375 and on XL50, pharmacokinetics of iHRANPs over a span of 24 h (PDF)

AUTHOR INFORMATION

Corresponding Authors

*E-mail: bingbozhang@tongji.edu.cn.
*E-mail: wangxiuli_1400023@tongji.edu.cn.

ORCID

Bingbo Zhang: 0000-0002-0981-7071

Author Contributions

#P. Wang, W. Yang, and S. Shen contributed equally to this work.

Notes

The authors declare no competing financial interest.

ACKNOWLEDGMENTS

This work was supported by the National Natural Science Foundation of China (81872212, 81571742, 81871399, 81922035, 81801823, 11874286), the Science and Technology Innovation Plan of Shanghai Science and Technology Committee (19441904200), and the Fundamental Research Funds for the Central Universities (221201800101). We express sincere gratitude to Prof. Ronald Sroka from the Department of Urology, University of LMU, Munich, Germany, for revising the manuscript. Great thanks go to Dr. Fei Wu from the Department of Pathology, Shanghai Dermatology Hospital, for pathological analysis.

REFERENCES

(1) Bebe, F. N.; Hu, S.; Brown, T. L.; Tulp, O. L. Role, Extent, and Impact of Comorbidity on Prognosis and Survival in Advanced Metastatic Melanoma: A Review. *J. Clin. Aesthet. Dermatol.* **2019**, *12*, 16−23.

(2) Hartman, R. I.; Lin, J. Y. Cutaneous Melanoma-A Review in Detection, Staging, and Management. *Hematol. Oncol. Clin. North. Am.* **2019**, *33*, 25−38.

(3) Hyams, D. M.; Cook, R. W.; Buzaid, A. C. Identification of Risk in Cutaneous Melanoma Patients: Prognostic and Predictive Markers. *J. Surg. Oncol.* **2019**, *119*, 175−186.

(4) Keyal, U.; Bhatta, A. K.; Zhang, G.; Wang, X. L. Present and Future Perspectives of Photodynamic Therapy for Cutaneous Squamous Cell Carcinoma. *J. Am. Acad. Dermatol.* **2019**, *80*, 765−773.

(5) Bichakjian, C.; Armstrong, M.; Baum, C.; Bordeaux, J. S.; Brown, M.; Busam, K. J.; Eisen, D. B.; Iyengar, V.; Lober, C.; Margolis, D. J.; Messina, J.; Miller, A.; Miller, S.; Mostow, E.; Mowad, C.; Nehal, K.; Schmitt-Burr, K.; Sekulic, A.; Storrs, P.; Teng, J.; et al. Guidelines of

DOI: 10.1021/acsnano.9b04070
ACS Nano 2019, 13, 11168−11180

Care for theManagement of Basal Cell Carcinoma. *J. Am. Acad. Dermatol.* **2018**, *78*, 540−559.
(6) Alam, M.; Armstrong, A.; Baum, C.; Bordeaux, J. S.; Brown, M.; Busam, K. J.; Eisen, D. B.; Iyengar, V.; Lober, C.; Margolis, D. J.; Messina, J.; Miller, A.; Miller, S.; Mostow, E.; Mowad, C.; Nehal, K.; Schmitt-Burr, K.; Sekulic, A.; Storrs, P.; Teng, J.; et al. Guidelines of Care for the Management of Cutaneous Squamous Cell Carcinoma. *J. Am. Acad. Dermatol.* **2018**, *78*, 560−578.
(7) Mar, V. J.; Chamberlain, A. J.; Kelly, J. W.; Murray, W. K.; Thompson, J. F. Clinical Practice Guidelines for the Diagnosis and Management of Melanoma: Melanomas that Lack Classical Clinical Features. *Med. J. Aust.* **2017**, *207*, 348−350.
(8) Paolino, G.; Donati, M.; Didona, D.; Mercuri, S. R.; Cantisani, C. Histology of Non-Melanoma Skin Cancers: An Update. *Biomedicines* **2017**, *5*, 71−82.
(9) Potenza, C.; Bernardini, N.; Balduzzi, V.; Losco, L.; Mambrin, A.; Marchesiello, A.; Tolino, E.; Zuber, S.; Skroza, N.; Proietti, I. A Review of the Literature of Surgical and Nonsurgical Treatments of Invasive Squamous Cells Carcinoma. *BioMed Res. Int.* **2018**, *2018*, 1−9.
(10) Prado, G.; Svoboda, R. M.; Rigel, D. S. What's New in Melanoma. *Dermatol. Clin.* **2019**, *37*, 159−168.
(11) Wrobel, S.; Przybylo, M.; Stepien, E. The Clinical Trial Landscape for Melanoma Therapies. *J. Clin. Med.* **2019**, *8*, 368−381.
(12) Roma-Rodrigues, C.; Mendes, R.; Baptista, P. V.; Fernandes, A. R. Targeting Tumor Microenvironment for Cancer Therapy. *Int. J. Mol. Sci.* **2019**, *20*, 840−870.
(13) Vera, R. E.; Lamberti, M. J.; Rivarola, V. A.; RumieVittar, N. B. Developing Strategies to Predict Photodynamic Therapy Outcome: The Role of Melanoma Microenvironment. *Tumor Biol.* **2015**, *36*, 9127−9136.
(14) Nissinen, L.; Farshchian, M.; Riihilä, P.; Kähäri, V.-M. New Perspectives on Role of Tumor Microenvironment in Progression of Cutaneous Squamous Cell Carcinoma. *Cell Tissue Res.* **2016**, *365*, 691−702.
(15) Danhier, F.; Feron, O.; Préat, V. To Exploit the Tumor Microenvironment: Passive and Active Tumor Targeting of Nanocarriers for Anti-Cancer Drug Delivery. *J. Controlled Release* **2010**, *148*, 135−146.
(16) Gao, S.; Yang, D. J.; Fang, Y.; Lin, X. J.; Jin, X. C.; Wang, Q.; Wang, X. Y.; Ke, L. Y.; Shi, K. Engineering Nanoparticles for Targeted Remodeling of the Tumor Microenvironment to Improve Cancer Immunotherapy. *Theranostics* **2019**, *9*, 126−151.
(17) López-Lázaro, M. Dual Role of Hydrogen Peroxide in Cancer: Possible Relevance to Cancer Chemoprevention and Therapy. *Cancer Lett.* **2007**, *252*, 1−8.
(18) Webb, B. A.; Chimenti, M.; Jacobson, M. P.; Barber, D. L. Dysregulated pH: APerfect Storm for Cancer Progression. *Nat. Rev. Cancer* **2011**, *11*, 671−677.
(19) Lennicke, C.; Rahn, J.; Lichtenfels, R.; Wessjohann, L. A.; Seliger, B. Hydrogen Peroxide-Production, Fate and Role in Redox Signaling of Tumor Cells. *Cell Commun. Signaling* **2015**, *13*, 39−57.
(20) Policastro, L.; Molinari, B.; Larcher, F.; Blanco, P.; Podhajcer, O. L.; Costa, C. S.; Rojas, P.; Durán, H. Imbalance of Antioxidant Enzymes in Tumor Cells and Inhibition of Proliferation and Malignant Features by Scavenging Hydrogen Peroxide. *Mol. Carcinog.* **2004**, *39*, 103−113.
(21) Vander Heiden, M. G.; Cantley, L. C.; Thompson, C. B. Understanding the Warburg Effect: The Metabolic Requirements of Cell Proliferation. *Science* **2009**, *324*, 1029−1033.
(22) Szatrowski, T. P.; Nathan, C. F. Production of Large Amounts of Hydrogen Peroxide by Human Tumor Cells. *Cancer Res.* **1991**, *51*, 794−798.
(23) Ji, T. J.; Zhao, Y.; Ding, Y. P.; Nie, G. J. Using Functional Nanomaterials to Target and Regulate the Tumor Microenvironment: Diagnostic and Therapeutic Applications. *Adv. Mater.* **2013**, *25*, 3508−3525.
(24) Liu, J. J.; Liang, H. N.; Li, M. H.; Luo, Z.; Zhang, J. X.; Guo, X. M.; Cai, K. Y. Tumor Acidity Activating Multifunctional Nanoplatform for NIR-Mediated Multiple Enhanced Photodynamic and Photothermal Tumor Therapy. *Biomaterials* **2018**, *157*, 107−124.
(25) Liu, J. P.; Zhang, R.; Xu, Z. P. Nanoparticle-Based Nanomedicines to Promote Cancer Immunotherapy: Recent Advances and Future Directions. *Small* **2019**, *15*, 1900262.
(26) Yu, Z. Z.; Wang, M. M.; Pan, W.; Wang, H. Y.; Li, N.; Tang, B. Tumor Microenvironment-Triggered Fabrication of Gold Nanomachines for Tumor-Specific Photoacoustic Imaging and Photothermal Therapy. *Chem. Sci.* **2017**, *8*, 4896−4903.
(27) Zheng, D. W.; Li, B.; Xu, L.; Zhang, Q. L.; Fan, J. X.; Li, C. X.; Zhang, X. Z. Normalizing Tumor Microenvironment Based on Photosynthetic Abiotic/Biotic Nanoparticles. *ACS Nano* **2018**, *12*, 6218−6227.
(28) Lee, D. W.; Khaja, S.; Velasquez-Castano, J. C.; Dasari, M.; Sun, C.; Petros, J.; Taylor, W. R.; Murthy, N. *In Vivo* Imaging of Hydrogen Peroxide with Chemiluminescent Nanoparticles. *Nat. Mater.* **2007**, *6*, 765−769.
(29) Zhang, Y.; Wu, C. Y.; Zhou, X. J.; Wu, X. C.; Yang, Y. Q.; Wu, H. X.; Guo, S. W.; Zhang, J. Y. Graphene Quantum Dots/Gold Electrode and Its Application in Living Cell H_2O_2Detection. *Nanoscale* **2013**, *5*, 1816−1819.
(30) Li, C. T.; Pan, R. J.; Li, P. Y.; Guan, Q. H.; Ao, J. P.; Wang, K.; Xu, L.; Liang, X. F.; Jin, X.; Zhang, C.; Zhu, X. Y. Hydrogen Peroxide-Responsive Nanoprobe Assists Circulating Tumor Cell Identification and Colorectal Cancer Diagnosis. *Anal. Chem.* **2017**, *89*, 5966−5975.
(31) Wang, W. J.; Tang, H. B.; Wu, Y.; Zhang, Y. L.; Li, Z. H. Highly Electrocatalytic Biosensor Based on Hemin@AuNPs/Reduced Graphene Oxide/Chitosan Nanohybrids for Non-Enzymatic Ultrasensitive Detection of Hydrogen Peroxide in Living Cells. *Biosens. Bioelectron.* **2019**, *132*, 217−223.
(32) Chen, Q.; Liang, C.; Sun, X. Q.; Chen, J. W.; Yang, Z. J.; Zhao, H.; Feng, L. Z.; Liu, Z. H_2O_2-Responsive Liposomal Nanoprobe for Photoacoustic Inflammation Imaging and Tumor Theranostics*via In Vivo*Chromogenic Assay. *Proc. Natl. Acad. Sci. U. S. A.* **2017**, *114*, 5343−5348.
(33) Yang, W. T.; Shi, X. D.; Shi, Y. X.; Yao, D. F.; Chen, S. Z.; Zhou, X.; Zhang, B. B. Beyond the Roles in Biomimetic Chemistry: An Insight into the Intrinsic Catalytic Activity of an Enzyme for Tumor-Selective Phototheranostics. *ACS Nano* **2018**, *12*, 12169−12180.
(34) Zhang, G.; Palmer, G. M.; Dewhirst, M. W.; Fraser, C. L. A Dual-Emissive-Materials Design Concept Enables Tumour Hypoxia Imaging. *Nat. Mater.* **2009**, *8*, 747−751.
(35) Mi, P.; Kokuryo, D.; Cabral, H.; Wu, H. L.; Terada, Y.; Saga, T.; Aoki, I.; Nishiyama, N.; Kataoka, K. A pH-Activatable Nanoparticle with Signal-Amplification Capabilities for Non-Invasive Imaging of Tumour Malignancy. *Nat. Nanotechnol.* **2016**, *11*, 724−730.
(36) Williams, G. A.; Ishige, R.; Cromwell, O. R.; Chung, J.; Takahara, A.; Guan, Z. B. Mechanically Robust and Self-healable Superlattice Nanocomposites by Self-Assembly of Single-Component "Sticky" Polymer-Grafted Nanoparticles. *Adv. Mater.* **2015**, *27*, 3934−3941.
(37) An, F. F.; Zhang, X. H. Strategies for Preparing Albumin-Based Nanoparticles for Multifunctional Bioimaging and Drug Delivery. *Theranostics* **2017**, *7*, 3667−3689.
(38) Zhang, B. B.; Jin, H. T.; Yan, L.; Chen, B. D.; Liu, S. Y.; Shi, D. L. Bioinspired Synthesis of Gadolinium-Based Hybrid Nanoparticles as MRI Blood Pool Contrast Agents with High Relaxivity. *J. Mater. Chem.* **2012**, *22*, 14494−14501.
(39) Zhao, Y.; Peng, J.; Li, J. J.; Huang, L.; Yang, J. Y.; Huang, K.; Li, H. W.; Jiang, N.; Zheng, S. K.; Zhang, X. N.; Niu, Y. J.; Han, G. Tumor-Targeted and Clearable Human Protein-Based MRI Nanoprobes. *Nano Lett.* **2017**, *17*, 4096−4100.
(40) Liu, G. Y.; Zou, J. H.; Tang, Q. Y.; Yang, X. Y.; Zhang, Y. W.; Zhang, Q.; Huang, W.; Chen, P.; Shao, J. J.; Dong, X. C. Surface Modified Ti_3C_2MXene Nanosheets for Tumor Targeting Photothermal/Photodynamic/Chemo Synergistic Therapy. *ACS Appl. Mater. Interfaces* **2017**, *9*, 40077−40086.

DOI: 10.1021/acsnano.9b04070
ACS Nano 2019, 13, 11168−11180

(41) Wang, Y.; Huang, X. Y.; Tang, Y. Y.; Zou, J. H.; Wang, P.; Zhang, Y. W.; Si, W. L.; Huang, W.; Dong, X. C. A Light-Induced Nitric Oxide Controllable Release Nano-Platform Based on Diketopyrrolopyrrole Derivatives for pH-Responsive Photodynamic/Photothermal Synergistic Cancer Therapy. *Chem. Sci.* **2018**, *9*, 8103−8109.
(42) Liang, P. P.; Huang, X. Y.; Wang, Y.; Chen, D. P.; Ou, C. J.; Zhang, Q.; Shao, J. J.; Huang, W.; Dong, X. C. Tumor-Microenvironment-Responsive Nanoconjugate for Synergistic Antivascular Activity and Phototherapy. *ACS Nano* **2018**, *12*, 11446−11457.
(43) Yang, T.; Tang, Y. A.; Liu, L.; Lv, X. Y.; Wang, Q. L.; Ke, H. T.; Deng, Y. B.; Yang, H.; Yang, X. L.; Liu, G.; Zhao, Y. L.; Chen, H. B. Size-Dependent Ag_2S Nanodots for Second Near-Infrared Fluorescence/Photoacoustics Imaging and Simultaneous Photothermal Therapy. *ACS Nano* **2017**, *11*, 1848−1857.
(44) Wu, Q.; He, Z. G.; Wang, X.; Zhang, Q.; Wei, Q. C.; Ma, S. Q.; Ma, C.; Li, J. Y.; Wang, Q. G. Cascade Enzymes within Self-Assembled Hybrid Nanogel Mimicked Neutrophil Lysosomes for Singlet Oxygen Elevated Cancer Therapy. *Nat. Commun.* **2019**, *10*, 240−253.
(45) Fan, W. P.; Lu, N.; Huang, P.; Liu, Y.; Yang, Z.; Wang, S.; Yu, G. C.; Liu, Y. J.; Hu, J. K.; He, Q. J.; Qu, J. L.; Wang, T. F.; Chen, X. Y. Glucose-Responsive Sequential Generation of Hydrogen Peroxide and Nitric Oxide for Synergistic Cancer Starving-Like/Gas Therapy. *Angew. Chem., Int. Ed.* **2017**, *56*, 1229−1233.

DOI: 10.1021/acsnano.9b04070
ACS Nano 2019, 13, 11168−11180